Astronomy & Astrophysics manuscript no. output
July 13, 2026

The WISSHFUL program

The highest-redshift UFO discovered in a non-lensed QSO

G. Lanzuisi[1], L. Borrelli[2,1], E. Piconcelli[3], G. Chartas[4], A. Luminari[3], J. Reeves[5,6], V. Braito[5,6,7], E. Bertola[8], S. Bianchi[9], A. Comastri[1], M. Brusa[2,1], C. Vignali[2,1], F. Vito[1], S. Marchesi[2,1,10], M. Cappi[1], M. Dadina[1], L. Zappacosta[3], A. Tortosa[3], M. Bischetti[11], G. Vietri[12], F. Salvestrini[11,13], G. Bruni[14], M. Fanelli[14,15], E. Kammoun[16], X. Zhao[16], G. Matzeu[17], F. Tombesi[3,18,19], A. Marinucci[20], M. Gaspari[21], T. Misawa[22], and D. Stern[16]

(Affiliations can be found after the references)

Received 1/04/2026; accepted 16/06/2026

ABSTRACT

We present the first results from the WISSHFUL program, an *XMM-Newton* heritage program targeting luminous quasi-stellar objects (QSOs) at cosmic noon. We report on recent simultaneous *XMM-Newton* and *NuSTAR* observations of the super-Eddington accreting quasar WISSH13 at z=3.294, which provide the highest-quality broadband X-ray spectrum to date for a non-lensed QSO at this redshift. Physical modeling of the continuum reveals a soft photon index ($\Gamma \sim 2$) and strong reflection ($R \sim 1.4 - 1.8$), despite the weak narrow Fe emission, and a low high-energy cutoff ($E_{\rm cut} \sim 60 - 80$ keV, $kT_e = 15 - 20$ keV, depending on the model adopted). Most notably, we detect two significant absorption features (at confidence levels of 96.7% and 98.9%, respectively) at ~ 7.5 and ~ 10 keV in the rest-frame, interpreted as a blueshifted blend of Fe XXV Heα and Fe XXVI Lyα. These features indicate the presence of two kinematic components of a highly ionized, high-column ultrafast outflow (UFO) with a velocity of $v_{\rm out} \sim 0.1c$ and $v_{\rm out} \sim 0.3c$, respectively. The slower wind is consistently detected in an archival 2017 *XMM-Newton* observation, whereas the faster wind is detected only in 2024. This stratified and variable wind exhibits extreme energetics, with a mass outflow rate of $\dot{M}_{\rm out} \sim 20 M_\odot/yr$ (corresponding to 15% $\dot{M}_{\rm acc}$) for each component, and a kinetic power on the order of ~ 1 and $\sim 10\%$ of the bolometric luminosity, respectively. While this represents one of the most powerful UFOs ever detected, its kinetic power is a similar fraction of the QSO's bolometric luminosity compared to lower-redshift active galactic nuclei. We present several theoretical frameworks to explain the peculiar accretion and ejection properties of this remarkable QSO at cosmic noon.

Key words. Galaxies: active – Black hole physics – galaxies: nuclei – X-rays: galaxies – Quasars

1. Introduction

Multiphase and multiscale winds driven by active galactic nuclei (AGNs) are thought to play a fundamental role in shaping supermassive black hole (SMBH)–galaxy coevolution (King & Pounds 2015; Laha et al. 2021) by removing and/or heating the cold gas from the host galaxy, quenching the growth of both the SMBH and the stellar component (Hopkins et al. 2006), and possibly explaining the tight SMBH-host mass relation (e.g., Silk & Rees 1998; Magorrian et al. 1998). To be relevant for AGN–galaxy coevolution, AGN feedback must be most effective when both BH growth and star formation rates are at their peaks, i.e., $z \sim 2 - 4$ (Madau & Dickinson 2014; Aird et al. 2015).

Indeed, luminous quasi-stellar objects (QSOs) at cosmic noon ($z = 2 - 4$) exhibit significant evidence of powerful outflows, as highlighted by the WISSH quasar survey (e.g., Bischetti et al. 2017; Vietri et al. 2022). The WISSH sample consists of 85 type-1 hyper-luminous quasars with $47.2 \leq Log(L_{\rm bol}/[erg\ s^{-1}]) \leq 48.2$, accreting at $-1.5 \leq \log(\lambda_{\rm Edd}) \leq 0.5$, at $1.8 < z < 4.7$, excluding lensed and radio-loud sources. A large fraction of WISSH sources show broad, blueshifted CIV emission with outflow velocities of several thousand kilometers per second (Vietri et al. 2018), a high incidence of broad absorption lines in the UV (Bruni et al. 2019), and [OIII] mass outflow rates among the highest reported in the literature (Bischetti et al. 2017), in some cases spatially resolved (see also Bertola et al. in prep.).

The nuclear drivers of the large-scale outflows observed in different bands are thought to be winds with velocities exceeding $0.1c$, launched from the vicinity of the SMBH at inner accretion disk scales, also referred to as ultrafast outflows (UFOs, Tombesi et al. 2010). By depositing substantial amounts of momentum and energy at the center of the host galaxy, these fast winds should be able to impact the host ISM, producing shocks that expand to large scales as energy-driven winds, with a mass loading factor in theory large enough to completely remove the host gas reservoir (Zubovas & King 2012; Fabian 2012; Faucher-Giguère & Quataert 2012; Costa et al. 2014).

These nuclear, fast winds can be seen in the X-rays, as the highly ionized gas of which they are composed only imprints absorption features of highly ionized elements, the most prominent ones being FeXXV/XXVI at $6.7 - 7$ keV rest-frame (e.g., Tombesi et al. 2011). These features are now routinely observed in 30-40% of local Seyferts and low-z QSOs (Gofford et al. 2013; Matzeu et al. 2023), while our knowledge at high redshift and luminosity remains limited. In fact, their detection requires high-quality X-ray spectra, which are challenging to obtain beyond the local Universe, with the notable exception of a few highly luminous and/or lensed QSOs (Chartas et al. 2003; Lanzuisi et al. 2012; Vignali et al. 2015; Dadina et al. 2016; Bertola et al. 2020). Chartas et al. (2021) presented the first systematic characterization of UFOs at high redshift, based, however, on a small, highly biased sample of targets, mostly selected for being lensed (80% of the sample) and/or with broad or narrow absorption lines in their UV spectra (80% of the sample).

Article published by EDP Sciences, to be cited as https://doi.org/10.1051/0004-6361/202660183

Table 1: WISSH13 multiwavelength properties.

ID	SDSS-ID	z	Log($L_{\rm bol}$) erg s^{-1}	Log($M_{\rm BH}$) $M_\odot$	$\lambda_{\rm Edd}$	$\dot{M}_{\rm acc}$ $M_\odot/yr$	v^{max}_{CIV} (km/s)	$\dot{M}^{out}_{CIV}$ $M_\odot/yr$	$v^{max}_{[OIII]}$ (km/s)	$\dot{M}^{out}_{[OIII]}$ $M_\odot/yr$
(1)	(2)	(3)	(4)	(5)	(6)	(7)	(8)	(9)	(10)	(11)
WISSH13	J0900+4215	3.294	47.9	9.3	3.2	140	2580^{+130}_{-160}	3	2380 ± 180	3300

Notes. (1) WISSH ID; (2) SDSS ID; (3) Redshift; (4) Bolometric luminosity from SED fitting in Saccheo et al. (2023); (5) BH mass from Hβ and (6) Eddington ratio and (7) corresponding mass accretion rate from Bischetti et al. (2017); (8) CIV maximum outflow velocity and (9) Mass outflow rate from Vietri et al. (2018); (10) [OIII] maximum outflow velocity; and (11) Mass outflow rate from Bischetti et al. (2017).

The WISSHFUL *XMM-Newton* Multi-year Heritage Program (ID 094353, PI G. Lanzuisi) is one of the largest *XMM-Newton* approved programs and aims to tackle this problem by obtaining deep *XMM-Newton* observations, over three cycles (AO23-24-25), of a sample of 15 hyper-luminous ($L_{\rm bol} > 10^{47}$ erg/s), high-redshift ($z \sim 2-4$) quasars selected from the WISSH quasar sample (Martocchia et al. 2017; Degli Agosti et al. 2025). These observations are specifically designed to reliably identify absorption features associated with nuclear winds and UFOs, investigate the wind-launching mechanism, and characterize the physical properties of nuclear winds in this critical luminosity and redshift regime.

We also obtained hard X-ray coverage for the AO23 and AO24 WISSHFUL targets through simultaneous *NuSTAR* Cycle 10 (ID 61062, PI Lanzuisi) and Cycle 11 observations (ID 61162, PI Borrelli). This enables us to accurately constrain the high-energy continuum properties, such as the photon index, high-energy cutoff, and reflection fraction. These parameters are crucial not only for a more robust detection and characterization of UFOs, but also for understanding the coronal properties, such as optical depth and electron temperature, of these extreme AGNs (Dadina et al. 2016; Kammoun et al. 2017; Lanzuisi et al. 2019; Kammoun et al. 2023) and the potential connection with the presence of powerful outflows (Tortosa et al. 2024; Lanzuisi et al. 2024). In fact, evidence is mounting that the presence and strength of such winds are somehow connected with the accretion properties of the central SMBH. An anticorrelation between broad-line region (BLR) wind velocity and X-ray luminosity was found in the WISSH QSOs (Zappacosta et al. 2020; Degli Agosti et al. 2025), while a similar connection with photon index was found in z>6 QSOs in the HYPERION survey (Tortosa et al. 2024). Interestingly, faster large-scale ionized outflows seem to also be connected with soft X-ray spectra (Wang et al. 2016).

At the same time, a correlation between the photon index and Eddington ratio has been reported by several authors (Shemmer et al. 2008; Brightman et al. 2013; Liu et al. 2021 but see also Trakhtenbrot et al. 2017; Laurenti et al. 2022; Tortosa et al. 2022). Recently, Inayoshi et al. (2025) presented a theoretical framework for Comptonization in a super-Eddington accretion disk, powering nuclear radiation-driven outflows and resulting in optically thick, warm coronae that naturally lead to soft, weak X-ray emission. All these elements – high accretion rates, nuclear outflows, warm coronae, and soft emission – might, in fact, be related. Performing deep coordinated *XMM-Newton* and *NuSTAR* observations of highly accreting luminous QSOs at high z is one of the best currently available approaches to solving this puzzle.

Here, we present the first results from our program focusing on the analysis of the *XMM-Newton* and *NuSTAR* data for the first observed target, WISSH13 (RA=09:00:33.50, DEC=+42:15:47.00) at z=3.294 with $L_{\rm bol} = 8 \times 10^{47}$ erg/s (Saccheo et al. 2023). The main properties of the target are summarized in Table 1. The velocities of the BLR wind mapped by the CIV, and of the narrow-line region (NLR) wind mapped by the [OIII] emission line blue wings, are taken from Vietri et al. 2018 and Bischetti et al. 2017, respectively. The target exhibits a powerful kiloparsec-scale [OIII] outflow, and a CIV outflow with similar velocities but a modest mass outflow rate, due to the smaller radius assumed for the BLR wind, and with large uncertainties due to the superimposition of the BLR and outflow components. For all these reasons, in the following, only the [OIII] outflow is used as a tracer of the galaxy-scale outflow energetics.

WISSH13 is detected with LOFAR (150 MHz), uGMRT (670 MHz), and JVLA (3, 6, and 10 GHz) as unresolved, showing no hint of complex morphology on kiloparsec scales (Fanelli et al. in prep.). The radio luminosity is among the highest in the WISSH sample ($L_{1.4GHz} \sim 10^{25.5} W/Hz$), placing it nominally above the radio-loud threshold in absolute terms. However, using the classical definition of radio-loudness, $\mathcal{R} = L_{5GHz}/L_{4400\text{Å}} > 10$ (Kellermann et al. 1989), the source is radio quiet, with $\mathcal{R} = 1.27$, due to the extreme optical luminosity.

The paper is organized as follows: Section 2 describes the observations and data reduction; Section 3 reports on the spectral analysis and UFO search carried out on the X-ray spectra; Section 4.1 describes the UFO characterization and energetics; and in Section 5 we discuss the main results in the context of accretion and ejection models. We adopt the cosmological parameters $H_0 = 70$ km s^{-1} Mpc^{-1}, $\Omega_\Lambda = 0.73$, and $\Omega_m = 0.27$. Errors are given at a 90% confidence level.

2. Observations and data reduction

We obtained three *XMM-Newton* observations for WISSH 13 in October 2024 (see Table 2). The data were reduced using SAS version 21, applying the optimized procedure of Piconcelli et al. (2004) to maximize the signal-to-noise ratio (S/N) in a given band by iteratively selecting the optimal source extraction region and background threshold. This allowed us to retain $\sim$ 80% of the exposure time for Obs. XMM1, which was affected by moderate flaring for 70% of the observation. Obs. XMM2 and XMM3 show more standard flaring levels. Final extraction radii are 15–30 arcsec for pn and 15–23 arcsec for MOS (70–85% encircled energy at 1 keV). Ancillary response files were generated with arfgen, enabling applyabsfluxcorr=yes to improve the *XMM-Newton*/*NuSTAR* cross-calibration (Kang & Wang 2023). MOS1 and MOS2 data were then combined into a single spectrum, while the response matrices were averaged.

We also included in the analysis Obs. XMM0 (PI: G. Risaliti), taken in 2017 (corresponding to a rest-frame separation of 1.6 years). The same reduction procedure was applied, yielding a net exposure of 20 ks. The source was $\sim$ 1.5 times brighter in 2017 than in 2024. Combined, the X-ray data presented here represent the highest-quality X-ray spectra of a $z > 2$ non-lensed QSO obtained so far, with 1.3×10^4 total 0.3-10 keV *XMM-Newton* net

Table 2: *XMM-Newton* and *NuSTAR* observation breakdown.

Telescope (1)	ObsID (2)	Time (3)	Tot. exp. ks (4)	Instrument (5)	Clean exp. ks (6)	Net counts 2-10 keV (7)	S/N 2-10 keV (8)
XMM0	0803950601	2017-11-17	33	pn	20	1568	36.8
				MOS1/2	23	953	29.9
XMM1	0943530701	2024-10-12	65	pn	55	2341	42.8
				MOS1/2	62	1534	35.6
XMM2	0943530801	2024-10-22	30	pn	19	1118	31.4
				MOS1/2	24	690	25.2
XMM3	0943532701	2024-10-31	24	pn	19	913	28.3
				MOS1/2	23	572	23.0
						10-20 keV	10-20 keV
NuSTAR1	61062007002	2024-10-21	74	FPMA+B	74	227	8.0
NuSTAR2	61062007004	2024-10-21	60	FPMA+B	60	225	8.9

Notes. (1) Obs. Name ; (2) Obs. ID; (3) Observation date; (4) Total exposure time; (5) Instrument; (6) Clean exposure time; (7) Net counts; and (8) Signal-to-noise ratio in the 2 − 10 keV band for *XMM-Newton* and 10 − 20 keV band for *NuSTAR*.

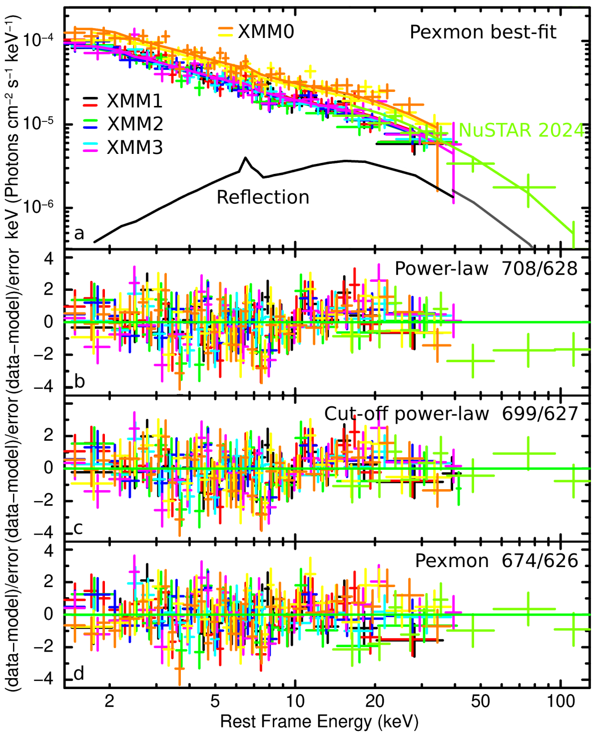

Fig. 1: Panel *a* shows the best-fit PEX model with the full *XMM-Newton* and *NuSTAR* dataset. pn and MOS1+2 data are shown with different colors for each observation, identified by its name. The reflection-only component is shown in black. Panels *b*, *c*, and *d* show residuals for the PL, CPL, and PEX models, respectively. Residuals for the REFL and CREFL models are not shown for clarity, as they are indistinguishable from those in panel d. C-stat/d.o.f. is reported for each model. *NuSTAR* FPMA and FPMB data are co-added for plotting purposes only.

counts and 5×10^3 in the 4-10 keV band rest-frame, comparable with local QSOs at z=0.1-0.5 in the SUBWAYS sample (Matzeu et al. 2023).

As part of a *NuSTAR* Cycle 10 follow-up program, we obtained two simultaneous observations of 74 and 60 ks alongside XMM2. The data were processed with NuSTARDAS v2 (Heasoft v.6.30)[1] and CALDB v20220316 using standard filtering. Background spectra were extracted from an annular region (100–210 arcsec), while the source extraction radius of 50 arcsec (∼ 65% encircled energy; An et al. 2014) was chosen to optimize the S/N in the 3–20 keV band, yielding 520 total net counts and a S/N of 15.

The *XMM-Newton* and *NuSTAR* spectra were binned following the Kaastra & Bleeker (2016) binning scheme to ensure optimal spectral resolution given the source and background flux levels (see Matzeu et al. 2023; Lanzuisi et al. 2024). The spectra were analyzed using the XSPEC software package (version 12.14.1 Arnaud 1996). The C−stat statistics (Cash 1979), with background subtraction (W-stat in XSPEC) was adopted during spectral fitting.

[1] `https://heasarc.nasa.gov/lheasoft/`

3. Spectral analysis

After verifying that the continuum spectral shape is consistent between the two epochs, we performed a joint broadband spectral analysis of WISSH13, simultaneously fitting the 2024 and 2017 *XMM-Newton* pn and MOS data, together with the 2024 *NuSTAR* FPMA and FPMB data. In all the models described below, we included a multiplicative constant component, free to vary across datasets, to account for cross-calibration and variability between the *XMM-Newton* and *NuSTAR* cameras. The value of this normalization constant was always between 0.9 and 1.1 between *XMM-Newton* pn and MOS and *NuSTAR* FPMA and FPMB cameras in the 2024 observations, in line with expected cross-calibration systematic uncertainties, while the 2017 *XMM-Newton* data have systematically higher normalization due to long-term flux variation. We also include Galactic absorption, modeled with a fixed $N_{\rm H}^{\rm Gal} = 2.3 \times 10^{20}\,{\rm cm}^{-2}$ (HI4PI Collaboration et al. 2016), while intrinsic absorption was not needed in any model.

3.1. Continuum modeling

We fit the combined *XMM-Newton* and *NuSTAR* spectra using several physically motivated models, listed below. The adopted continuum models are: i) a simple power-law model (`tbabs*zpowerlw`, PL) with free parameters the photon index, Γ, and normalization; ii) a power law with a high-energy cutoff at the source redshift, a cutoff power-law (`tbabs*cutoffpl`, CPL), with free parameters Γ, the high-energy cutoff, $E_{\rm cut}$, and normalization; iii) a cold reflection model using pexmon (Nandra et al. 2007), (`tbabs*pexmon`, PEX) with free parameters Γ, $E_{\rm cut}$, the reflection

Table 3: Best-fit parameters for the continuum models.

Parameter	PL	CPL	PEX	REFL	CREFL
(1)	(2)	(3)	(4)	(5)	(6)
Γ	$1.98^{+0.02}_{-0.02}$	$2.00^{+0.03}_{-0.03}$	$2.11^{+0.08}_{-0.07}$	$2.10^{+0.05}_{-0.03}$	-
E_{cut} [keV]	-	33^{+9}_{-4}	63^{+38}_{-18}	$79.5^{+28.9}_{-15.3}$	-
R	-	-	$1.8^{+0.9}_{-0.7}$	$1.4^{+0.7}_{-0.6}$	1.7 ± 0.5^{a}
kT_e [keV]	-	-	-	-	$17.4^{+17.7}_{-4.3}$
τ	-	-	-	-	$1.4^{+0.4}_{-0.7}$
C-stat/d.o.f.	708/628	699/627	674/626	681/626	679/626
$p_{MC}{}^{b}$	0.02	0.31	0.44	0.35	0.45
Model sign.^{c}	-	99.7	> 99.9	> 99.9	> 99.9
$F_{0.5-10}{}^{d}$	$2.07 \pm 0.09\ (3.5 \pm 0.2) \times 10^{-13}$				
$L_{2-10}{}^{d}$	$1.11 \pm 0.03\ (1.72 \pm 0.06) \times 10^{46}$				

Notes. (1) Model parameters referring to: (2) the power-law model; (3) the cutoff power-law model; (4) the `pexmon` model; (5) the `xillver` model; and (6) the `compTT+xillverCP` model.
$^{(a)}$ Reflection fraction computed from the flux ratio between the primary and reflected components in the 20–40 keV rest frame band and scaled to R units.
$^{(b)}$ Null hypothesis probability from Monte Carlo simulations. The simple power law model is rejected at a 98% confidence level, while the other models are all statistically acceptable.
$^{(c)}$ Significance in % of the improvement over the simpler model. See text for details.
$^{(d)}$ Average 2024 (2017) 0.5–10 keV flux and 2–10 keV rest-frame luminosity. They are consistent across the different models.

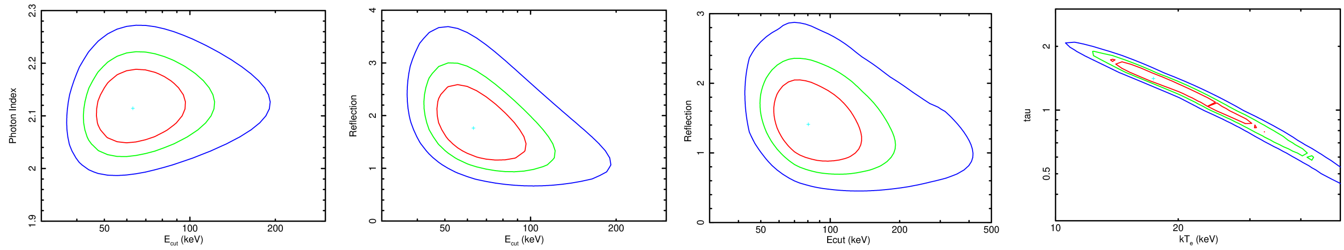

Fig. 2: From left to right: Confidence contours of E_{cut} vs. Γ; E_{cut} vs. R for the PEX model; E_{cut} and R for the REFL model; and kT_e and τ for the CREFL model. Red, green, and blue contours show 68, 90, and 99% confidence levels, respectively. The latter reveals a strong $\tau - kT_e$ degeneracy: higher kT_e is compensated for by lower τ (and vice versa), to reproduce the same observed photon index, Γ.

parameter R (> 0 so that the model also includes the primary power-law continuum) and normalization; iv) a cold reflection model using xillver (García & Kallman 2010; García et al. 2013), (`tbabs*xillver`, REFL) with free parameters Γ, E_{cut}, R (> 0 as for PEX, and normalization, where the ionization parameter is set to $log(\xi) = 0$, given the lack of evidence for ionized reflection; v) a Comptonization plus reflection model using compTT (Titarchuk 1994) (`tbabs*(compTT + xillverCP)`, CREFL) with free parameters the coronal electron temperature, kT$_e$, and the coronal optical depth, τ. The geometry was set to "slab" and the disk seed photon temperature to 100 eV. To reproduce the reflection in this model, we added a xillverCP component in reflection ($R = -1$), where the electron temperature of the corona was linked to the temperature in compTT, the normalization was free to vary, the photon index was set to $\Gamma = 2.0$, consistent with the observed value from previous models, and the ionization parameter was $log(\xi) = 0$. All the reflection components have the inclination angle parameter set to 30°, an average value for face-on, type-1 QSOs.

For the PEX, REFL, and CREFL models, the Fe abundance parameter, which regulates the Fe emission lines strength with respect to a given reflection spectrum, is set to 0.5 Solar. This choice was motivated by the weak emission observed at 6.4 keV: the equivalent width of a narrow Gaussian line (σ = 10 eV) added to the simple PL model and centered at 6.4 keV is < 60 eV rest-frame. Indeed, when left free to vary, the Fe abundance best-fit gives an upper limit of $A_{Fe} \lesssim 0.6$ Solar in all models.

Figure 1 compares the spectral residuals of the various models tested, showing that the three models, including both high-energy cutoff and reflection, all provide a good description of the data. We report the best-fit parameters and statistics of each model in Table 3. We evaluated the goodness-of-fit using Monte Carlo simulations (1000 realizations) with the Anderson-Darling test statistic using the `goodness` command in XSPEC. The simple power-law model is rejected at the 98% confidence level ($p_{MC} = 0.02$). The inclusion of a high-energy cutoff significantly improves the fit, yielding a model that is formally acceptable ($p_{MC} = 0.31$ corresponding to 69% of realizations with lower observed statistics).

To quantify the significance of the additional continuum components, we employed the likelihood ratio test (LRT), assuming that the $\Delta C-$stat approximately follows a χ^2 distribution with degrees of freedom equal to the number of added parameters (Cash 1979). The addition of the high-energy cutoff going from PL to CPL reduces the C-statistic by $\Delta C-$stat = 9. This improvement is significant at the 99.7% level for the addition of one parameter. The further addition of a reflection component, going from CPL to the PEX, REFL, or CREFL model, reduces the C-statistic by $\Delta C-$stat $= 18 - 25$. In this case, the improvement is significant at the 99.9% level for one parameter, for all three models. Thus, while the cutoff power law provides a plausible global description of the continuum, the reflection component is statistically required to explain the spectral curvature in the hard X-ray band. We note that the lower E_{cut} value obtained with the simple cutoff power-law model (~ 33 keV) compared to the reflection models (~ 60 − 80 keV) is expected, as the spectral curvature introduced by the unmodeled reflection component is translated into an artificially lower cutoff energy (see e.g., Tortosa et al. 2018; Middei et al. 2019).

We also investigated parameter degeneracies using contour plots. Figure 2 shows the confidence contours for Γ versus E_{cut} and R versus E_{cut} for the PEX model in the top row. The three parameters are all well constrained, with the photon index being $\gtrsim 2$, $R \gtrsim 1$, and $E_{cut} \lesssim 200$ keV at a 99% confidence level. The bottom row displays the R versus E_{cut} contours for the REFL

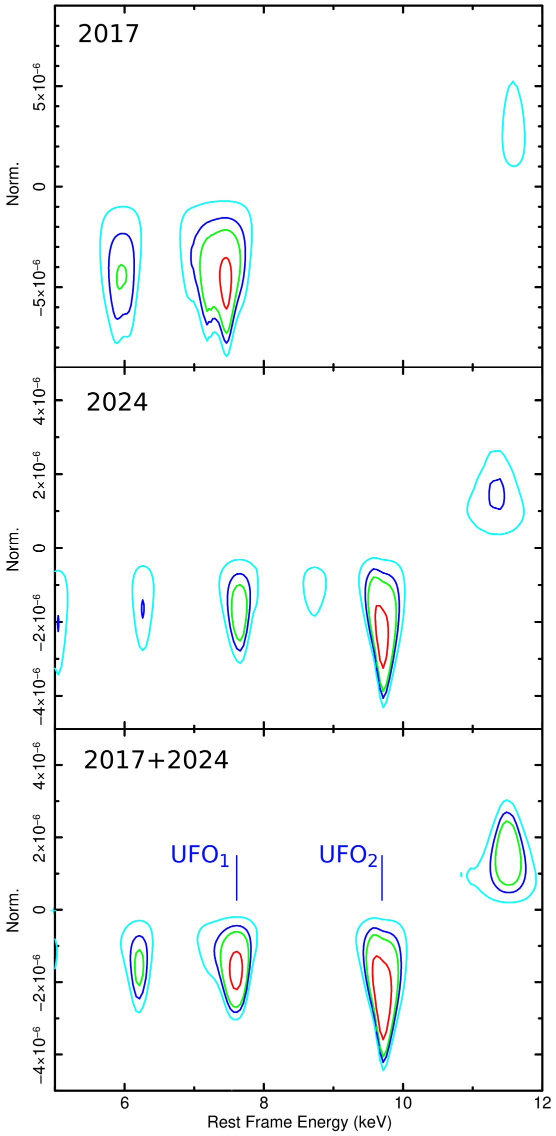

Fig. 3: Blind line scans over the 5–12 keV rest frame band. The plot shows contours of ΔC in the energy vs. line-normalization parameter space for a narrow Gaussian (σ = 10 eV) added to the baseline continuum. Cyan, blue, green, and red contours correspond to a ΔC of -2.3, -4.61, -5.99, and -9.21, respectively, which can be translated into a significance of 68, 90, 95, and 99% for two parameters.

model (left). This model shows a similar reflection and cutoff to PEX. Finally, the bottom right panel shows τ versus kT$_e$ for the CREFL model. As expected for thermal Comptonization, these two parameters are tightly anticorrelated, along a curve of a nearly constant Compton y parameter ($\propto kT_e \times \tau$) that reproduces the observed spectral slope, Γ (Tortosa et al. 2018; Middei et al. 2019).

The high-energy cutoff from PEX and REFL ($\sim 60 - 80$ keV) and the electron temperature from CREFL ($\sim$ 20 keV) agree within the errors with the typical scaling factor of $2 - 3$ (Petrucci et al. 2001; Middei et al. 2019) and consistently show that WISSH13 has one of the coolest coronal temperatures ever measured (Kara et al. 2017; Tortosa et al. 2017; Reeves et al. 2021; Bertola et al. 2022; Lanzuisi et al. 2024). The source accretion rate close to or above Eddington ($\lambda_{\rm Edd} \sim 3$, see Table 1) is in line with the observed trend of cooler coronae for highly accreting SMBHs observed in

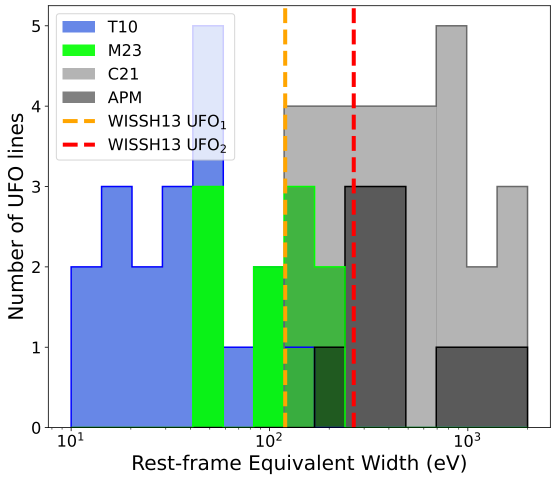

Fig. 4: Rest-frame equivalent widths for WISSH13 (dashed orange and red lines for UFO$_1$ and UFO$_2$, respectively) compared with Seyferts at $z < 0.1$ in blue (Tombesi et al. 2010, T10), QSOs at $z = 0.1 - 0.5$ in green (Matzeu et al. 2023, M23), and lensed, high-z QSOs in gray (Chartas et al. 2021, C21, and references therein), including the multiple detections in APM 08279+5255 (Chartas et al. 2009), shown in black.

Peluso et al. (2026) (but see also Zhao et al. 2026) on a sample of Seyferts and QSOs from the local Universe to cosmic noon, covering a wide range of BH masses ($log(M_{\rm BH}/[M_\odot]) = 6 - 10$) and luminosities ($log(L_{\rm bol}/[{\rm erg\ s^{-1}}]) = 42 - 48$).

3.2. Blind line search

We searched for the presence of any UFO-related absorption features superimposed on the best-fit continuum models described above. To estimate the energy, width, and significance of any absorption or emission feature relative to the underlying continuum, we conducted a blind search in the simultaneous fit of *XMM-Newton* and *NuSTAR* spectra, i.e., a blind Gaussian line scan across the Fe K band. We refer to Miniutti & Fabian (2006), Tombesi et al. (2010), Gofford et al. (2013), Matzeu et al. (2023), and Lanzuisi et al. (2024) for a similar approach.

We added a narrow Gaussian line (with line width fixed to σ = 10 eV, i.e., unresolved) to the underlying continuum modeled with PEX, which has the lowest $C-$stat value. However, we verified that consistent results are obtained by performing the same scan on the REFL or CREFL, i.e., the observed residuals are independent of the details of the primary emission and reflection spectral shapes. We allowed the power-law photon index and normalization to vary during the search. The reflection parameter and high-energy cutoff were fixed to their best-fit values to reduce the computational time. The scan was performed over the rest–frame $5 - 12$ keV interval for both emission and absorption features.

Since absorption features due to UFOs are known to be highly variable in time, changing centroid energy (i.e., velocity), and appearing and disappearing both on short (e.g., Cappi 2006; Chartas & Canas 2018; Braito et al. 2021) and long timescales (e.g., Saez & Chartas 2011; Matzeu et al. 2017; Bertola et al. 2022), we first performed the line scan on the *XMM-Newton* 2017 and 2024 spectra separately. In both cases, the 2024 *NuSTAR* spectra were included to help constrain the overall continuum shape and reflection intensity, and the best fit from the merged 2017+2024 spectra was used as a baseline. The resulting ΔC

Table 4: Best-fit parameters of the Gaussian components for UFO_1 and UFO_2 and statistical significance of the features.

	UFO_1	UFO_2
E (keV)	$7.6^{+0.1}_{-0.2}$	$9.8^{+0.1}_{-0.2}$
σ (keV)	< 0.39 (< 1.67)	< 0.29 (< 1.24)
Intensity	$-1.7^{+0.7}_{-0.9} \times 10^{-6}$	$-2.1^{+1.0}_{-1.2} \times 10^{-6}$
EW (eV)	28^{+15}_{-11} (120)	62^{+35}_{-29} (266)
ΔC-stat	9.8	11.7
$P_{\text{F-test}}$	99.0%	99.3%
$P_{\text{MonteCarlo}}$	96.7%	98.9%

Notes. Line energy is rest-frame; line width, σ, and equivalent width EW are in the observed frame, with rest-frame values in parentheses. σ upper limits are at a confidence level of 90%.

improvements over the baseline fit as a function of energy are shown in Figure 3 for the 2017 and 2024 spectra in the top and middle panels.

Two significant absorption features emerge: one at ~ 7.5 keV in the rest frame (~ 1.8 keV observed frame), detected at 99% and 95% confidence in 2017 and 2024, respectively, and one at ~ 9.7 keV (~ 2.3 keV observed frame), seen only in the 2024 spectra. For the ~ 7.5 keV feature, we performed a merged 2017+2024 scan to fully exploit the constraining power of the entire dataset, while for the ~ 9.7 keV feature, we ignored the 2017 spectrum between 9 and 10.5 keV. The results are shown in the bottom panel of Figure 3. By fitting a narrow, unresolved Gaussian line ($\sigma = 10$ eV) to the two strongest features in the joint fit, we obtained best-fit values for the first one (hereafter UFO_1), $E_{\text{rest}} = 7.6^{+0.1}_{-0.2}$ keV, with $\Delta C = 9.8$ and a single-trial F–test probability of 98.97%. The observed-frame equivalent width is EW $= 28^{+15}_{-11}$ eV, corresponding to ~ 120 eV in the rest frame. The second feature (UFO_2 hereafter) lies at $E_{\text{rest}} = 9.8^{+0.1}_{-0.2}$ keV with $\Delta C = 11.7$ and an F–test probability of 99.25%; its observed-frame equivalent width is EW $= 62^{+35}_{-29}$ eV (about 260 eV rest–frame). The best-fit values for the two Gaussian components are reported in Table 4, in which we also report the constraints on the line width obtained by leaving σ as a free parameter.

Single-trial F–test probability is known to overestimate the significance of line detections, as it does not consider the full energy range over which a line might be observed by chance, the so-called "look-elsewhere" effect (Protassov et al. 2002). Therefore, a full set of Monte Carlo (MC) simulations was performed to properly assess the significance of the detected features. Details are reported in Appendix A. Briefly, we simulated line-free *XMM-Newton* and *NuSTAR* spectra from the best-fit continuum with the same set of exposures of the real data, re-fit them with and without a narrow Gaussian line free to vary in intensity (both positive and negative) and energy in the full $5-12$ keV range, and stored the best-fit $C-$stat values with and without it. This shows the distribution of spurious ΔC peaks over the 5–12 keV range. Comparing the observed ΔC values to this distribution yields global confidences of 96.73% for UFO_1 and 98.86% for UFO_2, and therefore both features can be considered statistically significant, following the threshold adopted in, for example, Tombesi et al. (2010), Gofford et al. (2013), and Matzeu et al. (2023).

We verified that the detected absorption features are not driven by instrument systematics in the observed $\sim 1.8-2.3$ keV range. In particular, fitting the pn and MOS spectra separately yields

Table 5: XSTAR table best-fit parameters.

	UFO_1	UFO_2
$\log N_H$ (cm^{-2})	$23.8^{+0.5}_{-1.4}$	$24.1^{+0.3}_{-0.9}$
$\log \xi$ (erg cm s^{-1})	> 3.7	> 3.8
z_o	$2.94^{+0.09}_{-0.17}$	$2.06^{+0.07}_{-0.07}$
v_{out} (c)	$0.09^{+0.04}_{-0.02}$	$0.33^{+0.02}_{-0.02}$
ΔC-stat	9.8	11.3

Notes. v_{turb} is fixed to 5000 km s^{-1} for both UFO tables. v_{out} is derived from the best fit z values; see text for details.

consistent line energies and comparable improvements in the fit statistic, and the result remains stable against variations in the source and background extraction choices and flare-screening thresholds. In addition, no analogous residual is present in the corresponding background spectra around the line energies.

Figure 4 compares the observed EWs of UFO_1 and UFO_2 with literature samples. The WISSH13 features lie at the upper limit of the distributions for low-z Seyferts ($z < 0.1$, Tombesi et al. 2010) and local QSOs ($z = 0.1-0.5$, Matzeu et al. 2023), and below the larger EWs commonly reported at high redshift ($z = 1-4$, Chartas et al. 2021 and references therein). This highlights the importance and power of long, dedicated spectroscopic campaigns in high-z QSOs to go beyond the detection of the most extreme UFOs we have known so far, and explore what is most probably the bulk of the UFO population, showing properties analogous to the low-z AGN population, or alternatively test whether there is a real evolution in redshift and/or luminosity of such properties. We note that one third of the EW measurements for the high-z sample in Chartas et al. (2021) come from the persistent pair of UFO features observed in the extreme case of APM 08279+5255 (Chartas et al. 2009), which may further bias the distribution.

4. Properties of the UFO

4.1. Physical properties

We modeled the two absorption complexes with photoionized absorption tables computed with XSTAR, adopting a power-law ionizing SED matched to the measured continuum, with $\Gamma = 2$, in line with the observed value, and $L_{\text{ion}} = 6 \times 10^{46}$ erg s^{-1}, extrapolated from the observed spectrum to the 1-1000 Ryd band, i.e., $0.0136-13.6$ keV. We explored the parameter space $N_H = [10^{20} - 3 \times 10^{24}]$ cm^{-2} in 20 steps and $\log(\xi/\text{erg cm s}^{-1}) = [1-6]$ in 20 steps. We used as input parameters a gas density of 10^9 cm^{-3} and a temperature of 1×10^6 K, and set the remaining parameters to their default values within XSTAR. After several tests we adopted a table with input turbulent velocity $v_{turb} = 5000$ km s^{-1}, which is consistent with what is obtained in a fit with turbulent velocity as a free parameter (~ 4800 km/s for UFO_1 and ~ 4500 km/s for UFO_2) and is in agreement with the upper limits on σ shown in Table 4: $v_{turb} = 5000$ km s^{-1} corresponds to a σ of $\sim 40-50$ eV observed-frame at 2 keV.

We fit UFO_1 simultaneously in the full band joint fit, and UFO_2 only to the 2024 dataset, leaving the column density, N_H, ionization parameter, $\log \xi$, and absorber redshift, z, free to vary for both tables. Figure 5 shows the 68, 90, and 99% confidence contours in the $\log(N_H)$–$\log(\xi)$ plane for each component, while Table 5 reports the best-fit values.

For both XSTAR tables, the column density is constrained to be up to $N_H = 1-2 \times 10^{24}$ cm^{-2}, i.e., in the Compton thick regime, but with large uncertainties toward lower values, while the ionization

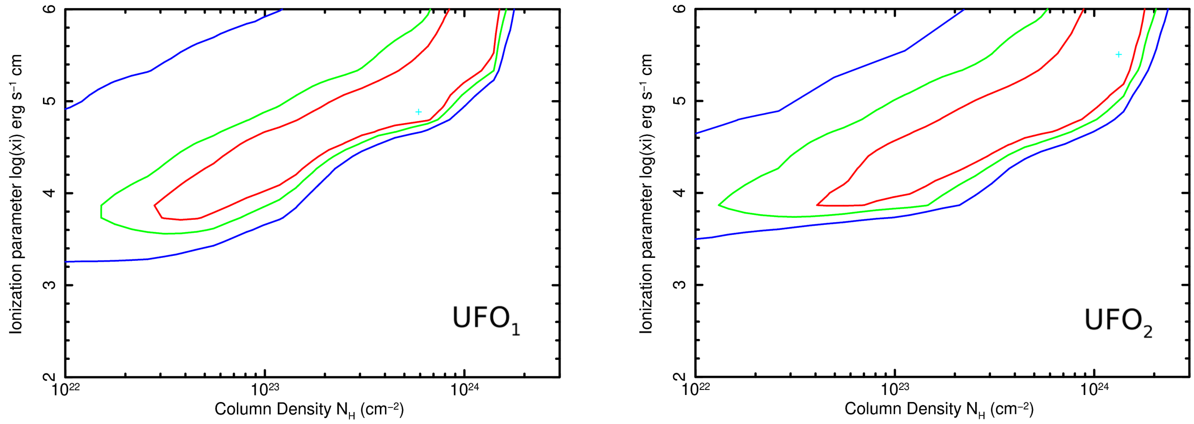

Fig. 5: Confidence contours (at 68, 90, and 99% confidence levels) for $\log N_{\rm H}$ vs. $\log\xi$ for UFO$_1$ (left) and UFO$_2$ (right) from the fit with XSTAR tables with $v_{\rm turb}$ = 5000 km s^{-1}.

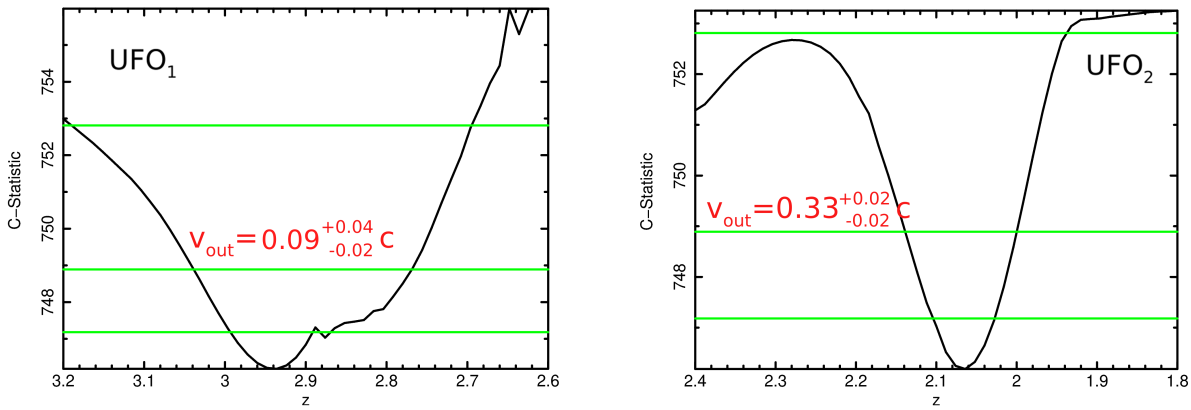

Fig. 6: Redshift contours from the fit with XSTAR tables with $v_{\rm turb}$ = 5000 km s^{-1}, for UFO$_1$ (left) and UFO$_2$ (right). The horizontal green lines mark the 68, 90, and 99% confidence levels. The 90% constraints on z were converted to $v_{\rm out}$ values quoted in the red labels (see text for details).

parameter is constrained only as a lower limit ($\log(\xi) > 3.5-4$ erg cm s^{-1}) as it reaches the upper boundary explored by the adopted XSTAR table, ($\log(\xi)$ = 6 erg cm s^{-1}). The improvement in the fit statistic is comparable to that obtained with a single Gaussian line for each UFO (Table 4), indicating that each XSTAR component produces a single blended Fe XXV/XXVI absorption feature that essentially fits each of the observed absorption troughs.

For both tables, $\log(N_{\rm H})$ and $\log(\xi)$ are strongly correlated (Figure 5), as higher ionization states produce weaker absorption troughs that, in turn, can accommodate larger columns to fit the same observed features. This is commonly seen in low-resolution spectra, where the different Fe ions features are blended, and it is not possible to fit them separately (Matzeu et al. 2016; Lanzuisi et al. 2024). For comparison, high-resolution data allow for a significantly more accurate derivation of $\log(\xi)$, and hence $\log(N_{\rm H})$, in addition to revealing multiple kinematic components in the wind, as in the cases of PDS456 (Xrism Collaboration et al. 2025), PG1211+143 (Mizumoto et al. 2026), IRAS05189–2524 (Noda et al. 2025), and NGC4151 (Xiang et al. 2025).

We note that the confidence intervals reported in Table 5 are the 1D 90% errors for one interesting parameter ($\Delta\chi^2$ = 2.706), while the contour plots in Figure 5 show the 2D 90% joint confidence regions for two interesting parameters ($\Delta\chi^2$ = 4.605, Avni 1976), which naturally encompass a broader range along each axis, particularly for correlated parameters. The reported results refer to the fit where the model is reproduced with PEX. However, consistent results are obtained in the other two cases, REFL and CREFL.

Finally, Figure 6 shows the redshift contours from the same fit, with the relative 68, 90, and 99% confidence levels. The z constraints were converted to $v_{\rm out}$ values using the Doppler formula $1+z_a = ((1+\beta)/(1-\beta))^{1/2}$, where $\beta = v/c$ and the relation between intrinsic absorber redshift, z_a, observed redshift, z_o, and source cosmological redshift, z_c, is given by $(1+z_o) = (1+z_a)(1+z_c)$ (e.g., Tombesi et al. 2011). From the redshift constraints, we derived $v_{\rm out} = 0.09^{+0.04}_{-0.02}c$ for UFO$_1$ and $v_{\rm out} = 0.33^{+0.02}_{-0.02}c$ for UFO$_2$.

4.2. Energetics

To compute mass outflow rates and energetics for the two UFOs, the standard approach is based on deriving the absorber location, assuming it is bounded between the escape-radius lower limit and the photoionization upper limit,

$$r_{\rm min} = \frac{2GM_{\rm BH}}{v_{\rm out}^2}, \qquad r_{\rm max} = \frac{L_{\rm ion}}{\xi N_{\rm H}}, \tag{1}$$

with $L_{\rm ion}$ integrated over 1–1000 Ryd.

In the case of WISSH 13, the small errors on $v_{\rm out}$ for UFO$_1$, imply that $r_{\rm min}$ is tightly constrained at $r_{\rm min} = 9.2^{+1.2}_{-1.0}$ $R_{\rm S}$ (Schwarzschild radii) for UFO$_2$, while it covers a larger range for UFO$_1$: $r_{\rm min} = 123^{+84}_{-64}$ $R_{\rm S}$. On the other hand, given the poorer constraints on $\log(N_{\rm H})$ and $\log(\xi)$, $r_{\rm max}$ is loosely constrained to be larger than a few hundred Schwarzschild radii for UFO$_2$

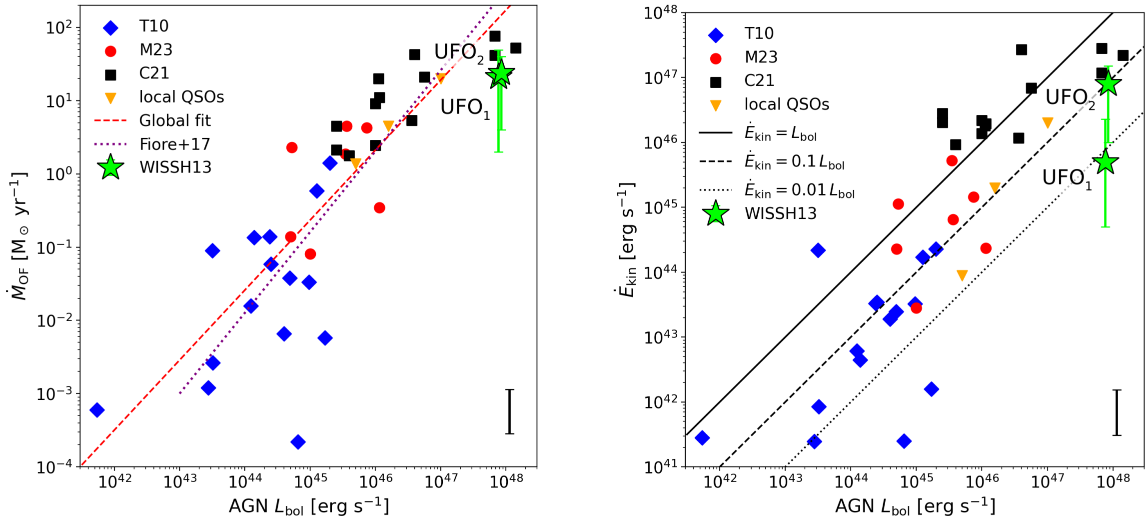

Fig. 7: UFO energetics for WISSH13 and literature samples: local Seyferts (T10, blue diamonds), low-z QSOs from SUBWAYS sample (M23, red circles), high-z lensed QSOs (C21, black squares), and local QSOs (PDS 456, IRASF 11119, and Mrk 231, see text for references, orange triangles). Left: $\dot{M}_{\rm out}$ vs. $L_{\rm bol}$. The dotted purple line is the relation derived in Fiore et al. (2017), while the dashed red line shows the linear fits obtained by jointly fitting all our data points. Right: $\dot{E}_{\rm kin}$ vs. $L_{\rm bol}$. Lines for $\dot{E}_{\rm kin} = 1, 0.1, 0.01 L_{\rm bol}$ are shown as continuous, dashed, and dotted lines, respectively. The average error bar on $\dot{M}_{\rm out}$ and $\dot{E}_{\rm kin}$ is shown on the bottom right of each plot.

and a few thousand for UFO$_1$. Therefore, in the following, as a conservative and often adopted approach, mass outflow rates and energetics are evaluated at $r_{\rm min}$ and treated as lower limits. We note that the escape-velocity assumption for $r_{\rm min}$ is clearly an oversimplification; however, the unresolved Fe K absorption and the absence of a P-Cygni profile prevent us from applying self-consistent disk-wind models (e.g., Matzeu et al. 2022; Luminari et al. 2024) that can directly constrain the launching radius, as has been done in nearby higher-S/N cases (e.g., Nardini et al. 2015; Reeves et al. 2024).

We accounted for the velocity–dependent reduction of the effective opacity at relativistic speeds, following the recipes in Luminari et al. 2020, 2024, i.e., a factor of ~ 1.2 at $v_{\rm out} = 0.09$c and ~ 2.0 at $v_{\rm out} = 0.33$c to recover the intrinsic $N_{\rm H}$ from the observed one. We adopted the outflow mass rate formula in Nardini & Zubovas 2018:

$$\dot{M}_{\rm out} = \Omega\, N_H\, m_p\, v_{\rm out}\, r, \tag{2}$$

where Ω is the global coverage fraction set to 0.5, m_p is the proton mass, and r is the radius adopted for the wind, which yields results equivalent to other widely used wind-mass formulae in the literature (e.g. Tombesi et al. 2011; Krongold et al. 2007).

Using the quantities reported in Table 5 and taking into account errors on $N_{\rm H}$ and $v_{\rm out}$, we derived a minimum mass outflow rate of $\dot{M}_{\rm out} = 21^{+28}_{-19}\ M_\odot$/yr ($\sim 0.15\ \dot{M}_{\rm acc}$) for UFO$_1$ and $\dot{M}_{\rm out} = 24^{+16}_{-20}\ M_\odot$/yr ($\sim 0.17\ \dot{M}_{\rm acc}$) for UFO$_2$. We note that, since log(ξ) is constrained only as a lower limit for both components, the strong log($N_{\rm H}$)-log(ξ) degeneracy implies that the true column densities could be systematically lower than the best-fit values reported in Table 6, which would in turn reduce the derived mass outflow rates beyond the statistical uncertainties quoted above. We also note that, given the definitions in Equation 1 and Equation 2, faster winds have significantly smaller radii (by a factor of 10 going from $v_{\rm out} = 0.1$ to $0.3c$) and the mass outflow rates effectively scale as $1/v_{\rm out}$. Taking into account relativistic correction and the different $N_{\rm H}$ values, the two winds end up having comparable mass outflow rates.

Table 6: UFO energetics for WISSH13.

Parameter	UFO$_1$	UFO$_2$
$r_{\rm min}$ ($R_{\rm S}$)	123^{+80}_{-64}	$9.2^{+1.2}_{-1.0}$
$\dot{M}_{\rm out}$ ($M_\odot$ yr^{-1})	21^{+28}_{-19}	24^{+16}_{-20}
$\dot{M}_{\rm out}/\dot{M}_{\rm acc}$	~ 0.15	~ 0.17
$\dot{E}_{\rm kin}$ (erg s^{-1})	$5^{+18}_{-4} \times 10^{45}$	$8^{+7}_{-7} \times 10^{46}$
$\dot{E}_{\rm kin}/L_{\rm bol}$	~ 0.006	~ 0.1
$\dot{P}_{\rm out}$ (dyn)	$3.5^{+3.4}_{-3.2} \times 10^{36}$	$1.6^{+1.2}_{-1.3} \times 10^{37}$
$\dot{P}_{\rm out}/(L_{\rm bol}/c)$	~ 0.14	~ 0.6

Notes. $R_{\rm S}$ stands for Schwarzschild radii. Energetics are computed at $r_{\rm min}$ and should be considered lower limits. Column densities are corrected for relativistic effects. A global covering fraction of $\Omega = 0.5$ is assumed.

Finally, we adopted the relativistic expressions for momentum and kinetic power:

$$\dot{P}_{\rm out} = \gamma \dot{M}_{\rm out} v_{\rm out}, \qquad \dot{E}_{\rm kin} = (\gamma - 1)\dot{M}_{\rm out} c^2, \tag{3}$$

where $\gamma = (1 - v_{\rm out}^2/c^2)^{-1/2}$. The derived quantities are summarized in Table 6.

Figure 7 compares $\dot{M}_{\rm out}$ (left) and $\dot{E}_{\rm kin}$ (right) of WISSH13 UFO$_1$ and UFO$_2$, as a function of $L_{\rm bol}$ compared with literature samples: local Seyferts from Tombesi et al. (2010), intermediate-redshift QSOs from the SUBWAYS sample (Matzeu et al. 2023), and high-z, mostly lensed QSOs from Chartas et al. (2021). The energetics for the Chartas et al. 2021 sample have been recomputed in Gianolli et al. (2024), using the same XSTAR table adopted in Matzeu et al. 2023, and assuming r_{min} as a radius, and should therefore be considered lower limits. We also added three well-studied low-z QSOs: PDS 456 (Nardini et al. 2015), IRASF 11119 (Nardini & Zubovas 2018; Lanzuisi et al. 2024), and Mrk 231 (Feruglio et al. 2015).

The values derived above place UFO$_1$ and UFO$_2$ in WISSH13 among the most massive and powerful UFOs known, in terms of the absolute mass outflow rate and kinetic energy (UFO$_2$ in particular). However, given the extreme luminosity and accretion

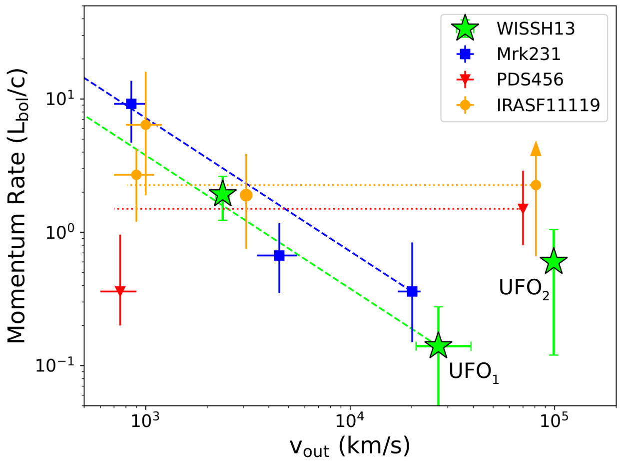

Fig. 8: Momentum rate vs. velocity of different outflow phases for WISSH13 (green stars), Mrk 231 (blue squares, Feruglio et al. 2015), PDS 456 (red triangles, Bischetti et al. 2019b), and IRASF 11119 (orange circles, Lanzuisi et al. 2024). Data points at $v_{\rm out} < 10^4$ km/s refer to either molecular outflows (CO or OH detection) or to [OIII] and UV winds. Data points at $v_{\rm out} > 10^4$ km/s refer to UFOs. Dotted horizontal lines show the evolution of a momentum-driven outflow in the case of PDS 456 and IRASF 11119, while dashed lines show the momentum boost expected for an energy-driven outflow in the case of Mrk 231 and WISSH13, if $\rm UFO_1$ is considered.

rate of WISSH13, when normalized to the QSO's $\dot{M}_{\rm acc}$ and $L_{\rm bol}$, they follow the relations between wind and accretion energetics observed over many orders of magnitude from the local Seyferts to the most powerful QSOs: over five orders of magnitude in $\dot{M}_{\rm acc}$ and six in $L_{\rm bol}$. UFOs in bright QSOs ($L_{\rm bol} > 10^{46}$ erg s^{-1}) seem to consistently carry at least $\sim$ 10% of the AGN accretion power, while lower-luminosity AGNs span a wider range, even going down to < 1%.

Finally, in Figure 8 we place WISSH13 in the multi–phase wind expansion context, where large-scale (molecular, ionized) outflow momentum rates are compared with those of nuclear outflows. A purely momentum-driven expansion implies momentum conservation over the wind expansion (dotted horizontal line), while in a purely energy-driven expansion, the wind-shocked bubble expands adiabatically, and should acquire a momentum boost inversely proportional to the difference in velocity ($P_{out} \propto v^{-1}$ dashed line; Zubovas & King 2012; Costa et al. 2014).

We compare WISSH13 with three local QSO and ultra-luminous infrared galaxy systems: Mrk 231, PDS 456, and IRASF 11119. These three systems span the full range of observed wind propagation mechanisms, from momentum-conserving (IRASF 11119, Veilleux et al. 2017; Lanzuisi et al. 2024) to energy-driven (Mrk 231, Feruglio et al. 2015) expansion, with PDS 456, dubbed "the gentle monster" (Bischetti et al. 2019b), showing a large-scale outflow momentum well below the well-studied, strong, and persistent nuclear wind (Nardini et al. 2015; Matzeu et al. 2016).

WISSH13 $\rm UFO_2$ appears among the fastest outflows for which such a comparison can be performed [2], but its momentum seems disconnected from that of the large–scale ionized outflow from [OIII] emission (Bischetti et al. 2017). Alternatively, the two winds can be reconciled under an energy-driven expansion if the coupling between the two is small, or if a significant fraction of the large-scale wind momentum is missed by only looking at the ionized phase (see Section 5.2). $\rm UFO_1$, on the other hand, seems to be in line with an energy-driven expansion, taking the large–scale outflow energetics at face value.

[2] With the exception of APM 08279+5255, where large uncertainties on the lensing factor greatly enhance uncertainties on wind energetics (Feruglio et al. 2017).

5. Discussion and conclusion

5.1. Accretion and ejection interplay

The continuum of WISSH13 is best described by a soft intrinsic spectrum with strong reflection and a notably low high-energy cutoff, corresponding to an unusually cold and moderately thick corona. The inferred electron temperature of $kT_{\rm e} \sim 20$ keV and optical depth of order unity place WISSH13 among the coldest coronae measured so far for luminous quasars, while its Eddington ratio, $\lambda_{\rm Edd} \sim 3$, clearly places it in the highly accreting regime. This behavior is consistent with the emerging trend of observationally colder coronae at higher luminosities and accretion rates (Peluso et al. 2026; Zhao et al. 2026) and with the idea that an increased UV- soft X-ray photon flux from the disk may efficiently cool the corona via Compton scattering, driving it toward a warm, optically thick state. This picture is further supported by the recent findings of Chen et al. (2025) based on stacked eROSITA spectra of ~4000 type-1 AGNs, who showed that the hot corona radius systematically decreases with increasing $\lambda_{\rm Edd}$ while remaining independent of $M_{\rm BH}$, consistent with the moderately thick and cold corona inferred for WISSH13 at $\lambda_{\rm Edd} \sim 3$.

Recent theoretical frameworks by Inayoshi et al. (2025) and Madau & Haardt (2024) present two distinct physical scenarios for the X-ray properties of super-Eddington accreting SMBHs such as WISSH13. Both models predict the formation of cold coronae coupled to radiation-driven outflows, qualitatively consistent with the low electron temperature ($kT_{\rm e} \sim 20$ keV) observed in WISSH13. However, reproducing the specific spectral slope of $\Gamma \sim 2$, rather than the extremely soft ($\Gamma > 3$) spectra typical of standard super-Eddington simulations, requires a specific configuration that distinguishes the two models. The Madau & Haardt (2024) model explicitly assumes an optically thin corona ($\tau = 0.5$) embedded deep within a reflective funnel. In this geometry, the corona is flooded by soft photons from the funnel walls, which cools the plasma so efficiently that the resulting spectrum is typically steep ($\Gamma \gtrsim 3$). Consequently, this model, in this simplified configuration, struggles to reproduce the $\Gamma \sim 2$ and moderate optical depth ($\tau \sim 2$) measured in WISSH13.

In contrast, the dynamic wind-corona model of Inayoshi et al. (2025) may provide a viable solution if the wind properties deviate from standard simulation predictions: super-Eddington simulations typically predict massive outflows comparable to the accretion rate (Hu et al. 2022; Jiang et al. 2019), leading to extremely high optical depths ($\tau_{\rm es} \gg 10$) that would suppress the hard X-ray continuum entirely. However, if the wind is not as massive as these theoretical models predict (a "starved" wind), as suggested by our rough estimates on $\dot{M}_{\rm out}$, the resulting corona would naturally have a significantly lower optical depth ($\tau_{\rm es} \sim 1-2$).

In this scenario, the wind opening angle is an adjustable parameter that can be tuned to match the observed τ: for a low-mass wind, moderate collimation can increase the effective density, boosting the optical depth, while a wider opening angle can accommodate a more massive wind. The WISSH13 could therefore be in a "sweet spot": accreting fast enough to drive a relativistic wind ($v_{\rm out} \sim 0.1-0.3c$) and cool the corona, but with a wind density tuned – by mass loading and/or collimation – to allow the hard X-ray continuum to emerge. This finding positions WISSH13 as a critical first case for testing these dynamic accretion-ejection models at cosmic noon.

5.2. A multi-component wind

The blind line search in the Fe K band reveals two significant absorption features, consistent with highly ionized gas outflowing at mildly relativistic speeds. Photoionization modeling confirms that the two features are associated with distinct wind signatures, with velocities of $v_{\rm out} \sim 0.1c$ and $v_{\rm out} \sim 0.3c$, both with high ionization and large column densities. Apart from the archetypal case of the lensed QSO APM 08279, this is the highest-redshift UFO detected to date. At the same time, the equivalent width of the absorption lines in WISSH13 lies at the upper envelope of the distributions for local Seyferts and at the lower end of those reported so far at high redshift. This indicates that long, dedicated spectroscopic campaigns on luminous high-z quasars allow us to move beyond the most extreme UFO detections and to start probing the bulk of the UFO population at cosmic noon, with properties more closely resembling those of low-z AGNs.

The detection of two distinct velocity components ($\sim 0.1c$ and $\sim 0.3c$) with different variability patterns suggests a complex, stratified outflow. We can quantify the expected variability behavior using the observability framework of King & Pounds (2015). They assume that UFOs are single thin shells launched instantaneously in each UFO episode, rather than continuous winds. The visibility window of a single shell then depends on its velocity and column density through their Equation 28:

$$t_{\rm off} = \frac{G M_{\rm BH}}{\Omega\, v_{\rm out}^3\, N_H\, \sigma_T} \simeq \frac{3\, M_7}{\Omega\, v_{0.1}^3\, N_{22}} \text{ month}, \quad (4)$$

where Ω is the covering factor, $v_{0.1} = v_{\rm out}/0.1c$, $N_{22} = N_H/10^{22}\,{\rm cm}^{-2}$, and $M_7 = M_{\rm BH}/10^7\,M_\odot$. For WISSH13 we obtain $t_{\rm off} \approx 2$ yr (rest-frame) for UFO$_1$ and $t_{\rm off} \approx 8$ days for UFO$_2$.

The large $t_{\rm off}$ for UFO$_1$ implies that a single shell remains detectable for $\lesssim 2$ yr after launch. Since UFO$_1$ is consistently detected across the two epochs (separated by ~ 1.6 yr rest-frame), the wind recurrence timescale must be $\lesssim t_{\rm off} \sim 2$ yr, ensuring that a detectable shell is always present along the line of sight. This naturally explains the consistent detection across the two epochs and supports its interpretation as a persistent, frequently relaunched wind streamline. In contrast, the very short $t_{\rm off} \sim 8$ days for UFO$_2$ implies that its shell disperses below detectability within days of launch. As was argued by King & Pounds (2015), the likelihood of detecting a UFO so shortly after launch is quite low. Therefore, the lack of detection in 2017 can be easily explained by the low probability of observing such a short-lived feature in any given observation.

This scenario is consistent with an episodic, transient origin for UFO$_2$, possibly triggered by magnetic reconnection events or flares near the inner disk surface, as recently observed by XRISM in NGC 3783 (Gu et al. 2025). Indeed, in the context of MHD wind models (Fukumura et al. 2010, 2017), the existence of a faster "spine" launched from the innermost regions of the accretion disk, surrounded by a slower "sheath" launched from larger radii, is predicted. The spine is highly sensitive to short-term fluctuations in the magnetic field configuration and is therefore expected to vary on timescales comparable to $t_{\rm flow}$.

Interestingly, the two-velocity structure observed in WISSH13 closely resembles the "UFO forest" recently resolved by XRISM/Resolve in PG 1211+143 (Mizumoto et al. 2026) and PDS 456 (Xrism Collaboration et al. 2025), where slower ($v \sim 0.1c$) winds from the outer accretion disk coexist with faster ($v \sim 0.3$–$0.4c$) winds from the inner slim-disk region. A similar behavior is reported in Bertola et al. (2020) for the Einstein Cross (the lensed QSO Q2237+030 at z=1.695), where the low-velocity UFO is recovered in all observations and through stacking, while the high-velocity one is only visible in some epochs. This emerging picture of a stratified, multi-velocity outflow as a common feature of near- and super-Eddington AGNs provides a natural physical framework for the UFO$_{1,2}$ detection in WISSH13. In this scenario, UFO$_1$ may be the primary long-term driver of feedback, while UFO$_2$ has a low duty cycle and therefore a limited impact on its surroundings. Consequently, when evaluating the momentum boost diagram (Figure 8), it is more useful to compare the momentum of the stable UFO$_1$ to the kiloparsec-scale ionized outflow. In this case, WISSH13 aligns well with an energy-conserving expansion scenario ($P_{out} \propto v^{-1}$), where the nuclear wind powers the kiloparsec-scale [OIII] outflow via adiabatic expansion (Zubovas & King 2012; Costa et al. 2014), while UFO$_2$ energetics are disconnected from or weakly coupled with those of the large-scale outflow.

Alternatively, UFO$_1$ could be interpreted as a failed wind (Proga & Kallman 2004; Giustini & Proga 2019). In this case, the gas is launched at a radius smaller than the escape radius for its observed velocity, causing it to stall and fall back toward the disk before escaping the nuclear region. In the slim-disk framework, radiation-driven winds are expected to be launched from the inner funnel at radii on the order of tens of Schwarzschild radii (Hu et al. 2022; Jiang et al. 2019), well below $r_{\rm min}$ for UFO$_1$, lending quantitative support to the failed-wind hypothesis for this component. If UFO$_1$ is indeed a failed outflow, its energetics (calculated assuming the wrong radius) are overestimated and, in any case, irrelevant for the momentum boost diagram, as it cannot interact with the galactic-scale feedback. Under this scenario, UFO$_2$ is the only potential driver for the large-scale outflow, and the comparison with the large-scale outflow in Figure 8 would be more in agreement with a small coupling between the two phases or a low-duty-cycle nuclear wind, in agreement with its transient nature.

Indeed, one proposed explanation for the heterogeneous distribution of momentum boosts in the literature invokes the time-variable nature of AGN accretion (Nardini & Zubovas 2018; Lanzuisi et al. 2024): the characteristic timescale for significant accretion rate variations ($\sim 10^4$–10^5 yr; e.g., Schawinski et al. 2015) is much shorter than the propagation timescale of the wind to kiloparsec scales ($\sim 10^6$–10^7 yr; e.g., Zubovas & Nardini 2020). As a consequence, the nuclear momentum flux fluctuates rapidly as the AGN flickers, while the large-scale side of Figure 8 records the time-averaged effect of many outflow episodes. We also note that the large-scale momentum rates derived from the [O III] ionized phase carry large uncertainties, as the ionized gas may trace only a fraction of the total outflowing mass, with the bulk likely residing in the molecular phase (e.g., Bischetti et al. 2019a; Travascio et al. 2024). A robust comparison of nuclear and galaxy-scale wind energetics therefore requires spatially resolved molecular gas observations.

Comparing the observed 1.4 GHz rest-frame luminosity with the radio power expected from wind-driven shocks using equation 32 from Nims et al. (2015), and adopting as kinetic luminosities $L_{\rm kin} = 5\times10^{-4}\,L_{\rm bol}$ from Bruni et al. (2019), the two are consistent with a wind coupling efficiency of $\sim 6\%$, just below the 7% threshold above which winds alone cannot account for the observed radio emission (Sun et al. 2017). However, we still cannot exclude the presence of a jet, possibly linked to the inner and faster UFO component (Fanelli et al. in prep.). Future VLBI studies will help us characterize the parsec-scale morphology and properties of QSOs, thereby distinguishing between wind and jet contributions.

5.3. Conclusions

In summary, WISSH13 is a laboratory for accretion and ejection under extreme conditions at $z \sim 3$, and it shows the potential of the recently approved WISSHFUL program to probe, in a systematic way, the interplay between accretion properties and nuclear outflows in the most luminous quasars at cosmic noon. Its cold, moderately thick corona, and the powerful variable nuclear wind may be examples of the physical conditions envisaged by recent models of super-Eddington accretion and radiation-driven outflows. Extending this type of analysis to the full WISSHFUL sample, in conjunction with other samples from the local Universe to the epoch of reionization, will provide a unique opportunity to understand how SMBH growth, coronal properties, and multiphase feedback are linked throughout the entire SMBH and host galaxy assembly history.

Within a self-regulated "BH-weather" cycle, turbulence-driven condensation and chaotic inflow lead to intermittent fueling episodes to which the corona and disk can respond rapidly (Gaspari et al. 2013, 2017; Wittor & Gaspari 2020). The emergence of a fast ionized outflow in 2024, absent in 2017, is qualitatively consistent with a duty cycle in which the wind is launched only during phases of enhanced accretion, motivating modeling strategies that allow the absorber strength to vary between epochs.

Advancing our understanding of nuclear wind properties requires new approaches: high-resolution X-ray spectroscopy with XRISM (XRISM Science Team 2020) is proving crucial to resolve the velocity structure and ionization stratification of the wind and break the $N_{\rm H}-\xi$ degeneracy that dominates the UFO energetics error budget. Results on PDS 456 (Xrism Collaboration et al. 2025) and NGC 3783 (Gu et al. 2025) already demonstrate the power of high spectral resolution to reveal multiple kinematic components and track wind acceleration in real time. For fainter high-z QSOs, such as those addressed in this work, we are currently limited to charge-coupled device (CCD)-like resolution. Only the future ESA L mission NewAthena (Cruise et al. 2025) will allow us to extend these studies from local Seyferts to highly accreting QSOs at cosmic noon and beyond, where accretion and ejection conditions are far more extreme — as demonstrated here for WISSH13 — and AGN feedback is potentially more impactful.

Acknowledgements. The authors acknowledge support from the INAF Large Program "DELUX" of the "Ricerca Fondamentale 2024" INAF program. EB acknowledges the support of the INAF GO grant "A JWST/MIRI MIRACLE: Mid-IR Activity of Circumnuclear Line Emission" and of the "Ricerca Fondamentale 2024" INAF program (mini-grant 1.05.24.07.01). T.M. acknowledges financial support from the JSPS KAKENHI grant No. 25K01038 "Comprehensive study of the feedback efficiency of AGN outflows to host galaxies". M.G. acknowledges support from the ERC Consolidator Grant *BlackHoleWeather* (101086804). FS acknowledges financial support from the PRIN MUR 2022 2022TKPB2P - BIG-z, "Ricerca Fondamentale 2023" INAF grant 1.05.23.03.04 "ARCHIE ARchive Cosmic HI & ISM Evolution", "Ricerca Fondamentale 2024" INAF grant 1.05.24.07.01 "ECHOS", Bando Finanziamento ASI CI-UCO-DSR-2022-43 CUP:C93C25004260005 project "IBISCO: feedback and obscuration in local AGN".

References

Aird, J., Coil, A. L., Georgakakis, A., et al. 2015, MNRAS, 451, 1892
An, H., Madsen, K. K., Westergaard, N. J., et al. 2014, in Space Telescopes and Instrumentation, SPIE Conference Series, 91441Q
Arnaud, K. A. 1996, in Astronomical Society of the Pacific Conference Series, Vol. 101, Astronomical Data Analysis Software and Systems V, ed. G. H. Jacoby & J. Barnes, 17
Avni, Y. 1976, ApJ, 210, 642
Bertola, E., Dadina, M., Cappi, M., et al. 2020, A&A, 638, A136
Bertola, E., Vignali, C., Lanzuisi, G., et al. 2022, A&A, 662, A98
Bischetti, M., Maiolino, R., Carniani, S., et al. 2019a, A&A, 630, A59
Bischetti, M., Piconcelli, E., Feruglio, C., et al. 2019b, A&A, 628, A118
Bischetti, M., Piconcelli, E., Vietri, G., et al. 2017, A&A, 598, A122
Braito, V., Reeves, J. N., Severgnini, P., et al. 2021, MNRAS, 500, 291
Brightman, M., Silverman, J. D., Mainieri, V., et al. 2013, MNRAS, 433, 2485
Bruni, G., Piconcelli, E., Misawa, T., et al. 2019, A&A, 630, A111
Cappi, M. 2006, Astronomische Nachrichten, 327, 1012
Cash, W. 1979, ApJ, 228, 939
Chartas, G., Brandt, W. N., & Gallagher, S. C. 2003, ApJ, 595, 85
Chartas, G. & Canas, M. H. 2018, ApJ, 867, 103
Chartas, G., Cappi, M., Vignali, C., et al. 2021, ApJ, 920, 24
Chartas, G., Saez, C., Brandt, W. N., Giustini, M., & Garmire, G. P. 2009, ApJ, 706, 644
Chen, S.-J., Buchner, J., Liu, T., et al. 2025, A&A, 701, A144
Costa, T., Sijacki, D., & Haehnelt, M. G. 2014, MNRAS, 444, 2355
Cruise, M., Guainazzi, M., Aird, J., et al. 2025, Nature Astronomy, 9, 36
Dadina, M., Vignali, C., Cappi, M., et al. 2016, A&A, 592, A104
Degli Agosti, C., Vignali, C., Piconcelli, E., et al. 2025, A&A, 702, A114
Fabian, A. C. 2012, ARA&A, 50, 455
Faucher-Giguère, C.-A. & Quataert, E. 2012, MNRAS, 425, 605
Feruglio, C., Ferrara, A., Bischetti, M., et al. 2017, A&A, 608, A30
Feruglio, C., Fiore, F., Carniani, S., et al. 2015, A&A, 583, A99
Fiore, F., Feruglio, C., Shankar, F., et al. 2017, A&A, 601, A143
Fukumura, K., Kazanas, D., Contopoulos, I., & Behar, E. 2010, ApJ, 715, 636
Fukumura, K., Kazanas, D., Shrader, C., et al. 2017, Nature Astronomy, 1, 0062
García, J., Dauser, T., Reynolds, C. S., et al. 2013, ApJ, 768, 146
García, J. & Kallman, T. R. 2010, ApJ, 718, 695
Gaspari, M., Ruszkowski, M., & Oh, S. P. 2013, MNRAS, 432, 3401
Gaspari, M., Temi, P., & Brighenti, F. 2017, MNRAS, 466, 677
Gianolli, V. E., Bianchi, S., Petrucci, P.-O., et al. 2024, A&A, 687, A235
Giustini, M. & Proga, D. 2019, A&A, 630, A94
Gofford, J., Reeves, J. N., Tombesi, F., et al. 2013, MNRAS, 430, 60
Gu, L., Fukumura, K., Kaastra, J., et al. 2025, A&A, 704, A146
HI4PI Collaboration, Ben Bekhti, N., Flöer, L., et al. 2016, A&A, 594, A116
Hopkins, P. F., Hernquist, L., Cox, T. J., et al. 2006, ApJS, 163, 1
Hu, H., Inayoshi, K., Haiman, Z., et al. 2022, ApJ, 935, 140
Inayoshi, K., Kimura, S. S., & Noda, H. 2025, PASJ, 77, 811
Jiang, Y.-F., Stone, J. M., & Davis, S. W. 2019, ApJ, 880, 67
Kaastra, J. S. & Bleeker, J. A. M. 2016, A&A, 587, A151
Kammoun, E. S., Igo, Z., Miller, J. M., et al. 2023, MNRAS
Kammoun, E. S., Risaliti, G., Stern, D., et al. 2017, MNRAS, 465, 1665
Kang, J.-L. & Wang, J.-X. 2023, arXiv e-prints, arXiv:2311.15499
Kara, E., García, J. A., Lohfink, A., et al. 2017, MNRAS, 468, 3489
Kellermann, K. I., Sramek, R., Schmidt, M., Shaffer, D. B., & Green, R. 1989, AJ, 98, 1195
King, A. & Pounds, K. 2015, ARA&A, 53, 115
Krongold, Y., Nicastro, F., Elvis, M., et al. 2007, ApJ, 659, 1022
Laha, S., Reynolds, C. S., Reeves, J., et al. 2021, Nature Astronomy, 5, 13
Lanzuisi, G., Gilli, R., Cappi, M., et al. 2019, ApJ, 875, L20
Lanzuisi, G., Giustini, M., Cappi, M., et al. 2012, A&A, 544, A2
Lanzuisi, G., Matzeu, G., Baldini, P., et al. 2024, A&A, 689, A247
Laurenti, M., Piconcelli, E., Zappacosta, L., et al. 2022, A&A, 657, A57
Liu, H., Luo, B., Brandt, W. N., et al. 2021, ApJ, 910, 103
Luminari, A., Piconcelli, E., Tombesi, F., Nicastro, F., & Fiore, F. 2024, A&A, 691, A357
Luminari, A., Tombesi, F., Piconcelli, E., et al. 2020, A&A, 633, A55
Madau, P. & Dickinson, M. 2014, ARA&A, 52, 415
Madau, P. & Haardt, F. 2024, ApJ, 976, L24
Magorrian, J., Tremaine, S., Richstone, D., et al. 1998, AJ, 115, 2285
Martocchia, S., Piconcelli, E., Zappacosta, L., et al. 2017, A&A, 608, A51
Matzeu, G. A., Brusa, M., Lanzuisi, G., et al. 2023, A&A, 670, A182
Matzeu, G. A., Lieu, M., Costa, M. T., et al. 2022, MNRAS, 515, 6172
Matzeu, G. A., Reeves, J. N., Nardini, E., et al. 2016, MNRAS, 458, 1311
Matzeu, G. A., Reeves, J. N., Nardini, E., et al. 2017, MNRAS, 465, 2804
Middei, R., Bianchi, S., Marinucci, A., et al. 2019, A&A, 630, A131
Miniutti, G. & Fabian, A. C. 2006, MNRAS, 366, 115
Mizumoto, M., Reeves, J. N., Braito, V., et al. 2026, ApJ, 997, 219
Nandra, K., O'Neill, P. M., George, I. M., & Reeves, J. N. 2007, MNRAS, 382, 194
Nardini, E., Reeves, J. N., Gofford, J., et al. 2015, Science, 347, 860
Nardini, E. & Zubovas, K. 2018, MNRAS, 478, 2274
Nims, J., Quataert, E., & Faucher-Giguère, C.-A. 2015, MNRAS, 447, 3612
Noda, H., Yamada, S., Ogawa, S., et al. 2025, ApJ, 993, L53
Peluso, S., Lanzuisi, G., Comastri, A., et al. 2026, arXiv e-prints, arXiv:2603.18156, A&A, in press
Petrucci, P. O., Merloni, A., Fabian, A., Haardt, F., & Gallo, E. 2001, MNRAS, 328, 501
Piconcelli, E., Jimenez-Bailón, E., Guainazzi, M., et al. 2004, MNRAS, 351, 161

Proga, D. & Kallman, T. R. 2004, ApJ, 616, 688

Protassov, R., van Dyk, D. A., Connors, A., Kashyap, V. L., & Siemiginowska, A. 2002, ApJ, 571, 545

Reeves, J. N., Braito, V., Luminari, A., et al. 2024, ApJ, 974, 58

Reeves, J. N., Braito, V., Porquet, D., et al. 2021, MNRAS, 500, 1974

Saccheo, I., Bongiorno, A., Piconcelli, E., et al. 2023, A&A, 671, A34

Saez, C. & Chartas, G. 2011, ApJ, 737, 91

Schawinski, K., Koss, M., Berney, S., & Sartori, L. F. 2015, MNRAS, 451, 2517

Shemmer, O., Brandt, W. N., Netzer, H., Maiolino, R., & Kaspi, S. 2008, ApJ, 682, 81

Silk, J. & Rees, M. J. 1998, A&A, 331, L1

Sun, A.-L., Greene, J. E., & Zakamska, N. L. 2017, The Astrophysical Journal, 835, 222

Titarchuk, L. 1994, ApJ, 434, 570

Tombesi, F., Cappi, M., Reeves, J. N., et al. 2011, ApJ, 742, 44

Tombesi, F., Cappi, M., Reeves, J. N., et al. 2010, A&A, 521, A57

Tortosa, A., Bianchi, S., Marinucci, A., Matt, G., & Petrucci, P. O. 2018, A&A, 614, A37

Tortosa, A., Marinucci, A., Matt, G., et al. 2017, MNRAS, 466, 4193

Tortosa, A., Ricci, C., Tombesi, F., et al. 2022, MNRAS, 509, 3599

Tortosa, A., Zappacosta, L., Piconcelli, E., et al. 2024, A&A, 691, A235

Trakhtenbrot, B., Ricci, C., Koss, M. J., et al. 2017, MNRAS, 470, 800

Travascio, A., Piconcelli, E., Bischetti, M., et al. 2024, A&A, 686, A250

Veilleux, S., Bolatto, A., Tombesi, F., et al. 2017, ApJ, 843, 18

Vietri, G., Misawa, T., Piconcelli, E., et al. 2022, A&A, 668, A87

Vietri, G., Piconcelli, E., Bischetti, M., et al. 2018, A&A, 617, A81

Vignali, C., Iwasawa, K., Comastri, A., et al. 2015, A&A, 583, A141

Wang, J., Xu, D. W., & Wei, J. Y. 2016, AJ, 151, 81

Wittor, D. & Gaspari, M. 2020, MNRAS, 498, 4983

Xiang, X., Miller, J. M., Behar, E., et al. 2025, ApJ, 988, L54

Xrism Collaboration, Audard, M., Awaki, H., et al. 2025, Nature, 641, 1132

XRISM Science Team. 2020, Science with the X-ray Imaging and Spectroscopy Mission (XRISM)

Zappacosta, L., Piconcelli, E., Giustini, M., et al. 2020, A&A, 635, L5

Zhao, X., Kammoun, E., Ajello, M., et al. 2026, arXiv e-prints, arXiv:2603.11286, submitted to ApJ

Zubovas, K. & King, A. 2012, ApJ, 745, L34

Zubovas, K. & Nardini, E. 2020, MNRAS, 498, 3633

[1] INAF – Osservatorio di Astrofisica e Scienza dello Spazio di Bologna, Via Gobetti, 93/3, I-40129 Bologna, Italy, e-mail: giorgio.lanzuisi@inaf.it
[2] Department of Physics and Astronomy (DIFA), University of Bologna, Via Gobetti, 93/2, I-40129 Bologna, Italy
[3] INAF – Osservatorio Astronomico di Roma, Via Frascati 33, 00078, Monte Porzio Catone (Roma), Italy
[4] Department of Physics and Astronomy, College of Charleston, Charleston, SC, 29424, USA
[5] Institute for Astrophysics and Computational Sciences, Department of Physics, The Catholic University of America, Washington, DC 20064, USA
[6] INAF, Osservatorio Astronomico di Brera, Via Brera 20, I-20121 Milano, Italy
[7] Dipartimento di Fisica, Università di Trento, Via Sommarive 14, Trento 38123, Italy
[8] INAF - Osservatorio Astrofisico di Arcetri, Largo E. Fermi 5, I-50125, Florence, Italy
[9] Dipartimento di Matematica e Fisica, Università degli Studi Roma Tre, Via della Vasca Navale 84, I-00146, Roma, Italy
[10] Department of Physics and Astronomy, Clemson University, Kinard Lab of Physics, Clemson, SC 29634, USA
[11] INAF – Osservatorio Astronomico di Trieste, Via G.B. Tiepolo, 11, I-34143 Trieste, Italy
[12] INAF – Istituto di Astrofisica Spaziale e Fisica cosmica Milano, Via Alfonso Corti 12, 20133 Milano, Italy
[13] -IFPU, Institute for Fundamental Physics of the Universe, Via Beirut 2, 34014 Trieste, Italy
[14] INAF – Istituto di Astrofisica e Planetologia Spaziali, Via Fosso del Cavaliere 100, 00133 Roma, Italy
[15] Dipartimento di Fisica, Sapienza Università di Roma, Piazzale Aldo Moro 5, 00185 Rome, Italy
[16] Cahill Center for Astronomy & Astrophysics, California Institute of Technology, 1216 East California Boulevard, Pasadena, CA 91125, USA
[17] Quasar Science Resources SL for ESA, European Space Astronomy Centre (ESAC), Science Operations Department, 28692, Villanueva de la Cañada, Madrid, Spain
[18] Department of Physics, University of Rome 'Tor Vergata', Via della Ricerca Scientifica 1, I-00133 Rome, Italy
[19] INFN – Sezione di Roma "Tor Vergata", Via della Ricerca Scientifica 1, I-00133 Roma, Italy
[20] ASI – Agenzia Spaziale Italiana, Via del Politecnico snc, 00133 Rome, Italy
[21] Department of Physics, Informatics and Mathematics, University of Modena and Reggio Emilia, 41125 Modena, Italy
[22] School of General Education, Shinshu University, 3-1-1 Asahi, Matsumoto, Nagano 390-8621, Japan

Appendix A: Monte Carlo simulations

To assess the statistical significance of the absorption features at 7.6 keV and 9.7 keV, we performed extensive Monte Carlo simulations as described in Lanzuisi et al. (2024) and Matzeu et al. (2023). We simulated 10 000 sets of pn and MOS1+2 spectra for the four exposure times listed in Table 2. As a baseline model, we adopted the best-fit continuum model without any lines, then refit it simultaneously to each set of spectra, added a narrow Gaussian line in emission or absorption (normalization free to vary in the $[-1, +1]$ range), and searched for the most significant spurious feature for each set of spectra across the full $5-12$ keV band.

The resulting distribution of ΔC values, shown in Fig. A.1, is then compared to the observed ΔC from UFO_1 and UFO_2 in the actual data. The features at 7.6 and 9.7 keV are at 96.73% and 98.86% confidence thresholds, respectively, confirming their high statistical significance. These confidence levels are larger than the typical threshold adopted in systematic studies done at lower redshift, such as those reported in Tombesi et al. (2010) and Matzeu et al. (2023), where a confidence level threshold of 95% from Monte Carlo simulations is adopted. These results support the interpretation of these features as signatures of a powerful UFO, consistent with the detection of winds in other hyper-luminous QSOs at high redshift.

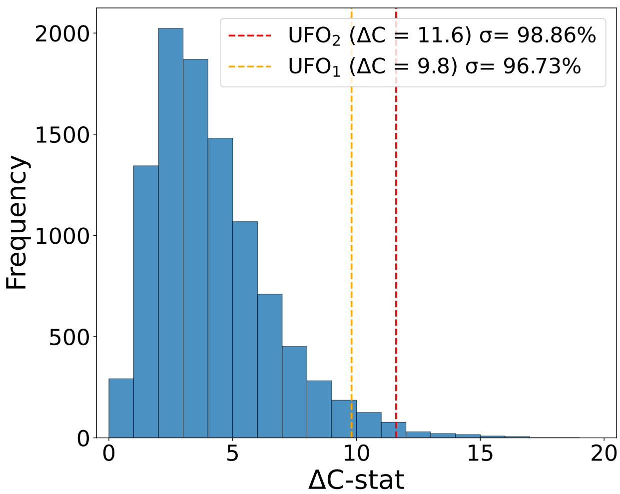

Fig. A.1: Distribution of ΔC from the Monte Carlo simulations. The observed ΔC for UFO_1 and UFO_2 are shown with orange and red vertical lines, respectively. The resulting significances are 96.73% and 98.86%, respectively.

Appendix B: Merged 2024 spectrum

For visualization purposes only, we show in Fig. B.1 the stacked spectra obtained by co-adding all 2024 EPIC-pn (black) and all MOS1+MOS2 data (red). The middle panel of Fig. B.1 shows the residuals without including two narrow Gaussian absorption lines, while the bottom panel shows residuals with the lines at the best-fit energies.

This stack is intended for illustrative purposes only: to avoid mixing different background levels and producing biased merged spectra, we must fully erase soft-proton flare intervals in all exposures before stacking. This requirement reduces the usable exposure time by $\sim 50\%$ with respect to the optimized reduction adopted in Sect. 2, significantly degrading the total number of counts and the S/N of the merged 2024 spectrum compared to the simultaneous joint fit on the individual 2024 spectra presented in Sect. 3.

The 2017 dataset, which makes the strongest contribution to the ~ 8 keV rest-frame feature associated with UFO_1, is not included in the stack. As a result, UFO_1 is only marginally recovered in the stacked representation, although it is robust in the joint fit. On the other hand, UFO_2 is clearly visible even in the stacked, lower-quality spectrum. We stress that pn and MOS1+2 show similar residuals at the same energy for both UFOs, further reinforcing our confidence in their detection.

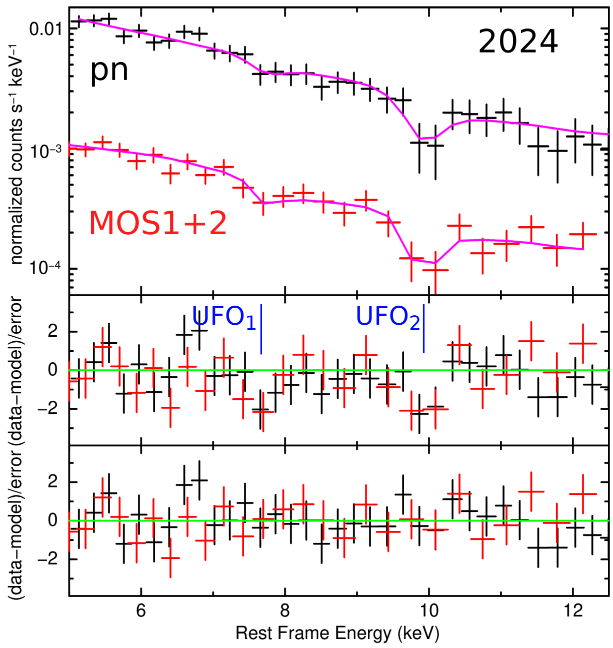

Fig. B.1: 2024 merged spectra: EPIC-pn (black) and MOS1+MOS2 (red). The best-fit model, including two absorption Gaussian lines, is shown in magenta. Middle: residuals without the two Gaussian absorption lines. Bottom: residuals with the two Gaussian absorption lines at the best-fit energy. The stack uses strictly flare-cleaned time intervals over the 2024 dataset to ensure comparable background levels among the stacked spectra, and therefore has lower exposure time and counts (by 50%) than the full, jointly fit 2024 spectra adopted in Sect. 3.